Enhanced Thermoelectric Performance in Oxide Composites of La and Nb Codoped SrTiO$_3$ by Using Graphite as the Electron Mobility Booster

Subhra Sourav Jana and Tanmoy Maiti*

Cite This: *ACS Appl. Mater. Interfaces* 2022, 14, 14174−14181
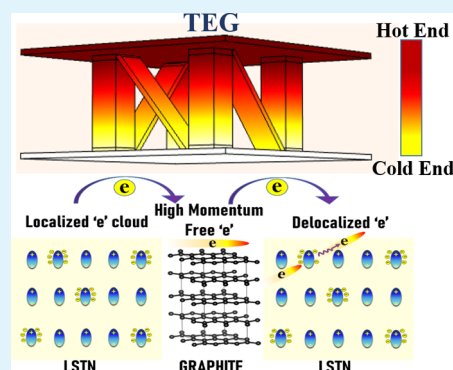
Read Online

ACCESS | Metrics & More | Article Recommendations | SI Supporting Information

ABSTRACT: Inherent insulating nature of oxides makes it challenging for use in thermoelectric applications that warrant reasonable electrical conductivity. In the present work, we have used graphite (G) to improve the electron transport in La$_{0.07}$Sr$_{0.93}$Ti$_{0.93}$Nb$_{0.07}$O$_3$ (LSTN) by making composites. Graphite acts as the electron momentum booster in the LSTN matrix, which otherwise suffers from Anderson localization of electrons, causing an order of magnitude increase in weighted mobility and electrical conductivity. As a result, the thermoelectric power factor increases more than 6 times due to graphite incorporation in LSTN. Furthermore, the lattice thermal conductivity is suppressed due to enhanced Umklapp scattering, as derived from the Debye−Callaway model. Hence, we have recorded ∼423% increment in the figure of merit (*ZT*) in LSTN + G composites. The maximum *ZT* obtained is 0.68 at 980 K for the LSTN with 1 wt % graphite composite. Furthermore, we have fabricated a four-legged n-type thermoelectric power generator demonstrating a milliwatt level power output, which hitherto remained unattainable for oxide thermoelectrics.

KEYWORDS: *thermoelectric, oxides, SrTiO$_3$, composite, graphite, perovskites*

INTRODUCTION

In light of current efforts toward solving environmental issues and energy crises, such as global warming and fossil fuel depletion, a thermoelectric generator (TEG) is considered to be one of the best solutions as it can directly convert waste heat into useful electrical energy without any carbon footprint. The performance of thermoelectric materials can be evaluated using the dimensionless figure of merit, ZT $(= S^2\sigma/\kappa\,T)$, where S is the Seebeck coefficient, σ is the electrical conductivity, and κ is the thermal conductivity comprising lattice (κ_l) and electronic (κ_e) contributions. Existing popular thermoelectric materials are narrow band gap semiconductors such as Bi- and Pb-based tellurides, selenides, and so forth.[1] Although these materials exhibit high ZT values, TEGs are yet to get widely commercialized because of their expensive and toxic constituents along with high-temperature instability. In contrast, oxide-based thermoelectrics have excellent thermal and chemical stabilities. SrTiO$_3$ (STO) is reported to be one of the most promising n-type oxide thermoelectrics for high-temperature applications, possessing large effective mass of electrons leading to a higher Seebeck coefficient.[2] However, its ZT values are found to be much inferior ($ZT < 0.4$) compared to those of chalcogenides due to poor electrical conductivity and large thermal conductivity. Over the years, a strategy of donor doping such as La and Nb has been employed to improve the electron transport behavior in STO. Codoping with donor atoms in A and B sites of the ABO$_3$ perovskite

structure of STO has been found to be one of the efficient ways to supply more electrons in the conduction band as well as to introduce more phonon scattering centers.[3,4] To date, the maximum ZT in n-type oxide thermoelectrics has been found to be 0.6 at 1100 K in La and Nb codoped STO systems.[3] It has been observed by researchers that chemical doping alone cannot increase ZT values significantly in STO due to interdependent thermoelectric parameters. A composite route, especially with carbon-based materials such as r-GO, GO, graphite, and so forth has been proven to be a successful strategy to enhance ZT.[5−13] In recent years, r-GO has been widely used to form a composite with doped STO demonstrating some of the excellent thermoelectric results among the n-type bulk oxide thermoelectrics.[5−9] The primary role of 2D graphene has been proposed to be enhancing the electron mobility by refining grain boundaries, which otherwise possess a highly resistive double Schottky barrier.[5,8,11] Due to depletion of oxygen vacancies at the grain boundary regions, this highly resistive Schottky barrier is formed in polycrystal-
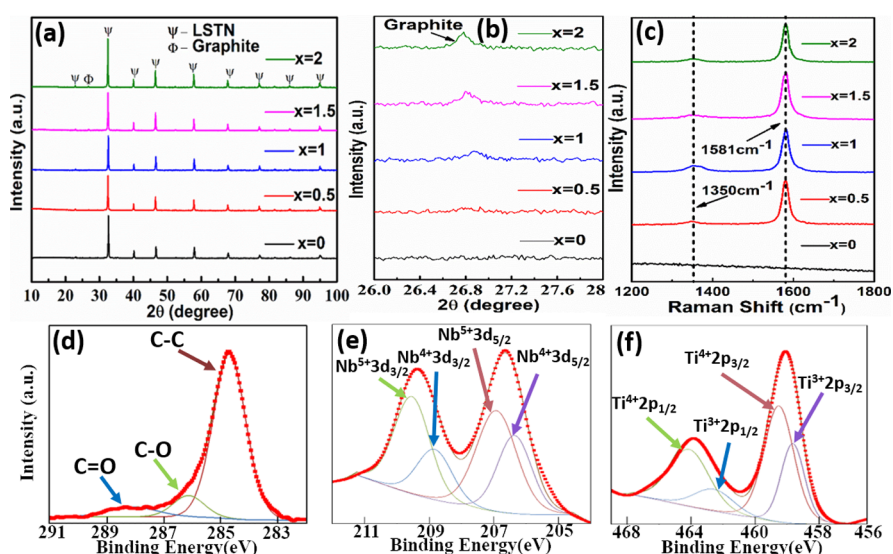
Figure 1. Microstructure and phase analysis: (a) XRD of all the LSTN + x wt % G compositions, (b) peak intensity of graphite in XRD, (c) Raman spectrum of LSTN + x wt % G, (d−f) XPS spectra of carbon, Nb, and Ti, respectively, for LSTN + 1 wt % G.

line oxide, which is further reduced due to the presence of 2D graphene as it promotes the formation of more oxygen vacancies.[8,11] As a result, single-crystal-like electron mobility is achieved in STO-based ceramics.[6−9,14] Although the concept of grain boundary engineering by highly conductive 2D materials such as graphene seems to be quite convincing, it always raises the concern whether it is the sole reason for observing single-crystal-like charge transport in spite of using a very small quantity (<1 wt %) of graphene, which may not cover the omnipresent grain boundaries in polycrystalline ceramics. Recently, Acharya et al. have reported ZT = 1.42 in the composite of Nb-doped STN with graphite, which infers a significant breakthrough in the field of oxide thermoelectrics for attaining the highest ever ZT among n-type oxide thermoelectrics.[12] Such a large ZT has been observed primarily due to a large increment in electrical conductivity without significant impact on the Seebeck coefficient due to graphite addition. Because graphite is present as grains or inclusions in the STN matrix unlike the segregation of 2D graphene in the grain boundaries, the grain boundary refinement cannot be the only reason behind such an improvement in electrical transport. Interestingly, these doped STOs show very poor conductivity in spite of having a large electron concentration. It is more likely that Anderson localization of electrons is present in these complex oxides due to variations in local electrical fields created by lattice defects, as reported by many in the literature.[15−20] However, the presence of graphite helps those electrons to become delocalized and causes a manifold increment in weighted mobility of electrons resulting in enhanced electron transport.

In the present work, $La_{0.07}Sr_{0.93}Ti_{0.93}Nb_{0.07}O_3$ (LSTN) is chosen as the parent material to form a composite with graphite as the maximum ZT obtained so far among doped STO systems has been for La and Nb codoped STO.[3,4] Graphite is found to be capable of significantly increasing the electrical conductivity by an order of magnitude in LSTN. Besides restraining lattice thermal conductivity by strong Umklapp scattering at elevated temperatures, it facilitates achieving a manifold increase in ZT values. Furthermore, a four-legged n-type TEG is fabricated using the best-performing LSTN + G composites, and 2.5 milliwatt of power output is

obtained, which is higher than the microwatt level of power output reported for oxide-based TEGs.[21]

■ RESULTS AND DISCUSSION

Microstructure and Phase Analysis. LSTN + G composites have been synthesized by the solid-state reaction using spark plasma sintering (SPS), which is known as the fast sintering technique. Details of the synthesis process are described in the Supporting Information. A cubic perovskite phase with a $pm\overline{3}m$ space group is obtained for pristine LSTN, which is retained even after graphite addition, as shown in Figure 1a,b. Rietveld analysis is performed using Fullprof software to estimate the lattice parameter, which is found to be 3.92 Å for LSTN and does not change much with the addition of graphite (Figure S1 and Tables S1 and S2). The presence of graphite is further confirmed by the Raman spectrum shown in Figure 1c. A sharp G band at 1581 cm^{-1} is a signature peak of graphitic carbon coming from the first-order phonon scattering of sp^2 carbon atoms.[22] In addition, a small peak is found at a Raman shift of 1350 cm^{-1} corresponding to the D band, which arises from structural defects. In the present study, D bands appear as a result of mechanical exfoliation[23] of graphite due to repeated nanomilling involved in the processing of these materials.[24,25] A small 2D band is found at a Raman shift of 2460 cm^{-1} along with a sharp 2G band at 2742 cm^{-1} as shown in Figure S2 in the Supporting Information. Hence, Raman spectroscopy as well as X-ray diffraction (XRD) confirm the retention of carbon in the form of graphite in these composites.

X-ray photoelectron spectroscopy (XPS) is performed to evaluate the binding energies of C, Nb, and Ti in the LSTN + 1 wt % G composite as shown in Figure 1d−f. The binding energies are tabulated in Table S3, which are found to be in good agreement with literature values.[26−30] It is inferred that more than 80% of the carbon is present in the pure graphitic form (C−C), whereas about 18% present with functional groups (C−O, C═O) mostly due to processing through nanomilling. Around 37% Nb is converted to Nb^{4+} to maintain the charge balance and about 68% of the Ti is able to retain Ti^{4+} for LSTN + 1 wt % G.
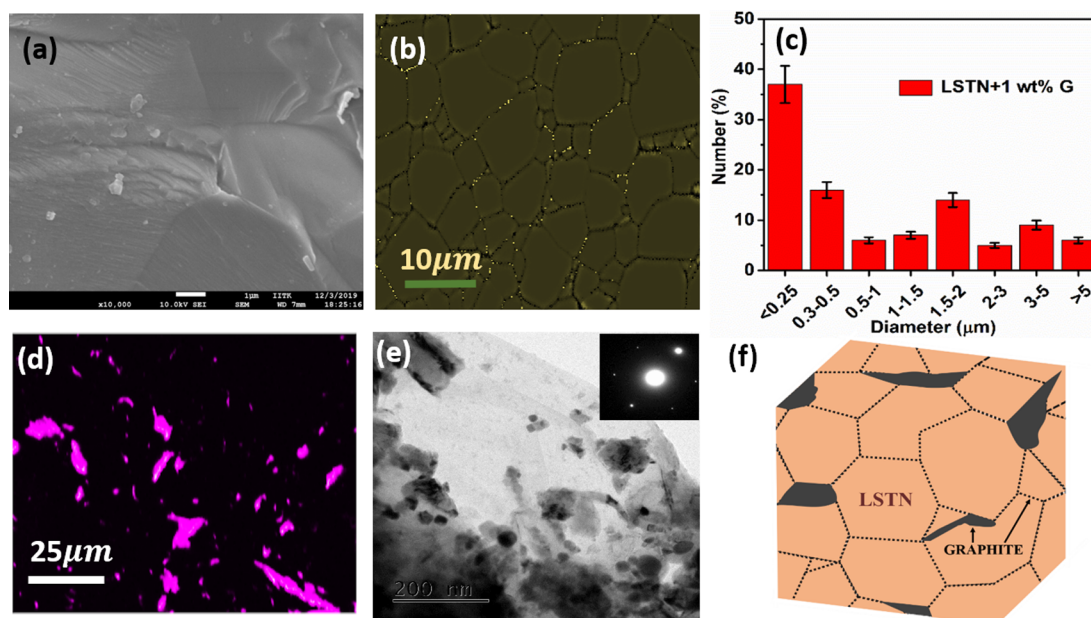
Figure 2. Microstructure of LSTN–graphite composites: (a) FESEM image showing a dense microstructure, (b) phase contrast image depicting a thin layer of graphite inclusions at the grain boundary, (c) grain size distribution of LSTN + 1 wt % G, and (d) surface elemental map of LSTN + 2 wt % G with the violet area pointing the agglomeration of graphite. (e) TEM image of dispersed LSTN particles in graphite flakes (SAED image of graphite in the inset) of LSTN + 1 wt % G and (f) schematic of the LSTN + graphite composite.
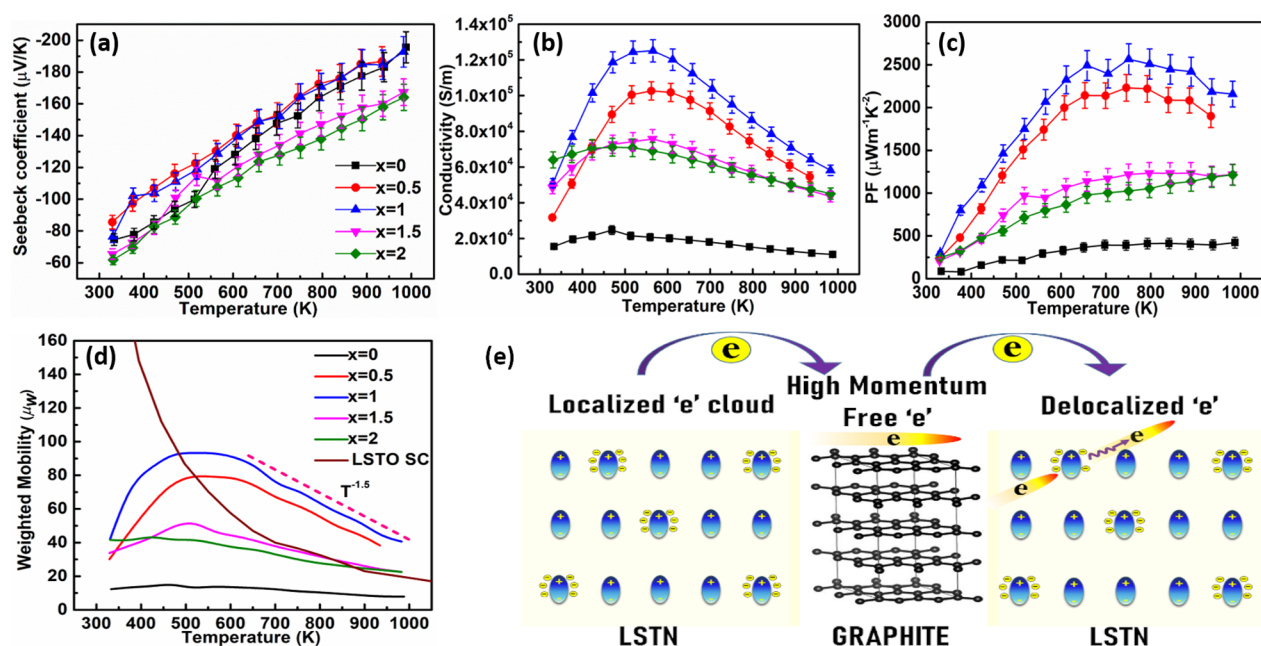

Figure 3. Electrical transport of LSTN + x wt % G; (a) Seebeck coefficient, (b) electrical conductivity, (c) power factor, (d) weighted mobility of all composites along with La-doped STO single crystals,[33] and (e) schematic of electrical transport of the LSTN + G composite.

The FESEM image in Figure 2a shows the dense microstructure of LSTN grains in LSTN + 1 wt % G. The phase contrast image of electron backscatter diffraction is shown in Figure 2b, where the lighter area depicts a fine layer of graphite inclusions present in the composites. The grain size of the as-synthesized LSTN + G composite shows a wide distribution from submicron size to as large as 5 μm as shown in Figure 2c. About 37% grains are available below 250 nm. This combination of small to large grains is an ideal recipe to balance the trade-off between thermal and electrical transport.

Elemental mapping of the LSTN + 1 wt % G composite performed by energy-dispersive X-ray spectrometry shown in Figure S3 in the Supporting Information indicates the homogeneous distribution of all the constituent elements. The number of large graphite particles or chunks increases as the graphite content increases to 2 wt % G, which is clearly visible in the elemental map shown in Figure 2d. Agglomerated fine LSTN particles on graphite flakes are observed in the transmission electron microscopy (TEM) image (Figure 2e) with the selected area electron diffraction (SAED) image of

graphite flakes in the inset. The schematic of the micro-structure of the LSTN−graphite composite is given in Figure 2f, where graphite is present in the grain boundary as well as large particles.

Electrical Transport. A negative Seebeck coefficient and its linear increase with temperature observed in all the samples signify n-type degenerate semiconductor-like behavior, as shown in Figure 3a. On the contrary, temperature dependence of electrical conductivity (σ) of all the compositions shows semiconductor-like behavior ($d\sigma/dT > 0$) at lower temperatures and metallic behavior ($d\sigma/dT < 0$) at elevated temperatures undergoing semiconductor to metal transition (S−M) near 450−600 K, as depicted in Figure 3b. The maximum electrical conductivity of 1.25×10^5 S/m has been found in LSTN + 1 wt % G, which is an order of magnitude higher than that of pristine LSTN with no significant deterioration in the Seebeck coefficient. As a result, we could enhance the power factor (PF) from 411 μW m^{-1} K^{-2} for pristine LSTN to 2566 μW m^{-1} K^{-2} by compositing with graphite, as shown in Figure 3c. In addition, thermoelectric parameters exhibit excellent cyclability during heating and cooling cycles as shown in Figure S5 in the Supporting Information. A barely minimum hysteresis (<0.1%) is observed in the cyclability data of the LSTN + G samples, which is very promising from the TEG device perspective.

To understand such a kind of amplification in electrical conductivity values due to incorporation of graphite, we have further estimated the band gaps of all the samples from Kubelka−Munk fitting of the UV−vis spectroscopy data shown in Figure S4 in the Supporting Information. Interestingly, not much change in the band gap is observed in LSTN due to graphite addition. As expected, the band gap is found to be in the range of (3.14−3.18) eV for all the composites as presented in Table S4. Hence, it is inferred that a significant increase in conductivity does not arise from the band gap reduction due to graphite addition. Hall measurement data presented in Table S5 further reveal that the electron concentration (n) of all the composites including pure LSTN remains on the order of 10^{20} cm^{-3}. Furthermore, effective mass of electrons ($m*$) is also estimated using the Pisarenko relation.[31,32]

$$\left(S = \frac{8\pi^2 k_B^2}{3eh^2} m* T \left(\frac{\pi}{3n} \right)^{2/3} \right) \tag{1}$$

The effective mass ranges between 0.6 and 0.8 for all the compositions are shown in Figure S6. It corroborates well with our observation that the Seebeck coefficient is not affected in spite of enormous surge in electrical conductivity. However, a minimal deviation in the carrier concentration, effective mass, and band gap does not really justify the significant increment of electrical conductivity, obtained in the composite samples. Hence, electron mobility plays a significant role in improving electrical transport of composites with graphite. For further elucidation, weighted mobility has been calculated using eq 2,[8] which suggests that conductivity at low temperatures is driven by thermally activated mobility.

$$\mu_w = \frac{3h^3\sigma}{8\pi e(2m_e k_B T)^{3/2}} \left[\frac{\exp\left[\frac{|S|}{k_B/e} - 2\right]}{1 + \exp\left[-5\left(\frac{|S|}{k_B/e} - 1\right)\right]} \right.$$

$$\left. + \frac{\frac{3}{\pi^2} \frac{|S|}{k_B/e}}{1 + \exp\left[5\left(\frac{|S|}{k_B/e} - 1\right)\right]} \right] \tag{2}$$

Polycrystalline pristine LSTN has expectedly quite lower μ_w with respect to single-crystal data[33] as shown in Figure 3d. A maximum μ_w of 93.3 cm^{-2} V^{-1} S^{-1} has been obtained for LSTN + 1 wt % G, which is around 6.7 times higher than that of the pristine LSTN. Furthermore, μ_w of the LSTN + 0.5 and 1 wt % G composite exceed the single-crystal value above 500 K. A high-temperature negative slope depicts the dominating behavior of acoustic phonon scattering. We compared with the single-crystal value of La-doped STO due to unavailability of single-crystal data for La and Nb co-doped STO in the literature.

Such a kind of enhancement in weighted mobility has been reported for the composites of STO doped with graphene, and the reason has been attributed to the reduction of the Schottky barrier height[5,8,11] in polycrystalline STO due to the segregation of highly conductive graphene along the grain boundaries. However, in the present scenario, unlike 2D graphene, graphite is located as flakes and inclusions distributed in the LSTN matrix as shown schematically in Figure 2f. However, the possibility of a small amount of oxygen vacancy generation by changing the oxygen diffusion kinetics near the grain boundary due to graphite incorporation cannot be ruled out, but this cannot be the only mechanism to increase the weighted mobility beyond the single-crystal level. Hence, we have looked deeper to find the reason behind the change in electrical conductivity in the LSTN + G composites from thermally activated electron transport at lower temperatures to metallic charge transport due to acoustic phonon scattering at high temperatures, above 500 K. It is reported in the literature that band models cannot really explain the charge transport mechanism in these oxide perovskites, which possess point defects arising from the presence of multivalent cations and processing of ceramics.[34−38] It is surprising to see that in spite of having an electron concentration on the order of 10^{20} cm^{-3}, which explicitly satisfies Mott criteria (in eq 3)[39] for the STO system (10^{18} cm^{-3}),[40] all the compositions including pristine LSTN exhibit semiconducting behavior near room temperature instead of showing metallic behavior.

$$a_B n^{1/3} \approx 0.25 \tag{3}$$

Here, a_B is the Bohr radius and n is the critical carrier concentration required for S−M transition. This kind of Mott transition has already been reported in many oxide perovskites.[10,12,41−44] It is possible that using codoping in STO and processing steps such as repeated calcination in a reducing atmosphere, nanomilling can generate a significant amount of defects and lattice strain, which render the electrons to be localized. This localization of the carrier is known as Anderson localization.[45−47] Anderson localization can be conceded as one of the possible explanations behind the oppressive electrical conductivity in pristine LSTN, which does not get reflected in the Hall measurement data.[48] Herein, we propose
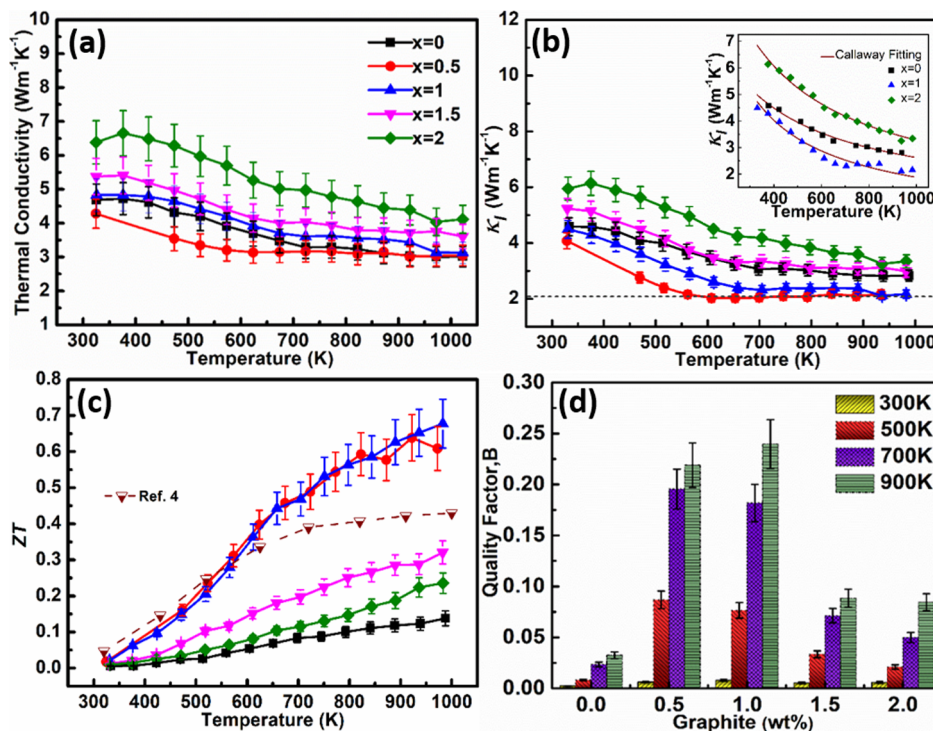
Figure 4. Thermal transport and thermoelectric performance: (a) total thermal conductivity, (b) lattice contribution of thermal conductivity, (c) ZT with the dotted line depicting the reported value[4] of La$_{0.07}$Sr$_{0.93}$Ti$_{0.93}$Nb$_{0.07}$O$_3$, and (d) quality factor of LSTN + x wt % G.

that graphite is basically working as the electron momentum booster in the LSTN + G composite system. Electrons are localized in the case of pristine LSTN resulting in a poor weighted mobility value as shown in Figure 3e. When some of the hot electrons transfer from LSTN grains to graphite, they travel faster through graphite particles as free electrons acquiring a larger momentum. High-energy or high-momentum electrons further coming out of graphite facilitate more electrons to acquire the itinerant state above the mobility edge in LSTN, which otherwise suffers from Anderson localization. Besides, it is believed that the presence of graphite in the LSTN matrix imparts enough strain to enable Anderson-localized electrons in LSTN to acquire the itinerant state above the mobility edge by overcoming the energy barrier. Meanwhile, the Seebeck coefficient is not affected by the electrons whether they are localized or delocalized,[49] hence the Seebeck coefficient is not deteriorated that much in spite of having more than five times increment in electrical conductivity. However, 1 wt % graphite concentration is proven to be the optimum concentration for increasing electrical conductivity and the power factor. An increase in the graphite concentration forms aggregation of graphite (Figure 2d), which tends to scatter electrons. We have found that when the graphite concentration becomes >1 wt %, the scattering mechanisms start to dominate and electrical conductivity is suppressed, which result in lowering of the power factor.

Thermal Transport. Thermal conductivity (Figure 4a) of pristine LSTN and its graphite composites has been estimated by measuring thermal diffusivity (D) and C_p ($\kappa = D_\rho C_p$) shown in Figure S7a,b. Furthermore, electronic thermal conductivity (κ_e) is calculated using the Wiedemann−Franz Law ($\kappa_e = L\sigma T$) shown in Figure S7c in the Supporting Information.[50] The shape of the κ_e curve (Figure S7d) for all the compositions is expectedly the replica of their electrical conductivity. κ_l of all

the samples is calculated by subtracting κ_e from total thermal conductivity. It is found that overall thermal conductivity is dominated by lattice thermal conductivity shown in Figure 4b, and that is the reason why the κ_e curve is overshadowed in the total thermal conductivity. The lowest theoretical lattice thermal conductivity of pure LSTN is ∼2 W m^{-1} K^{-1} as approximated using the Cahill model.[51] This limit of lattice thermal conductivity is reached for the LSTN + 0.5 wt % G composition that is about 2 W m^{-1} K^{-1} at 890 K, which is lower than that of pristine LSTN, 2.84 W m^{-1} K^{-1} at 890 K. A further increase in the graphite concentration leads to an increase in κ_l, which results maximum κ_l for the case of 2 wt % G. For a better understanding of phonon transport in the LSTN + G composites, κ_l is evaluated using the Debye− Callaway model (eq 4).[52]

$$\kappa_l = \frac{k_B}{2\pi^2 v}\left(\frac{k_B T}{\hbar}\right)^3 \int_0^{\theta_D/T} \frac{\tau(y, T)y^4 e^y}{(e^y - 1)^2}dy \qquad (4)$$

where $y = \hbar\omega/k_B T$, ω is the phonon frequency, $\hbar$ is the reduced Plank's constant, θ_D is the Debye temperature, v_m is the mean acoustic velocity, and τ is the relaxation time. Overall relaxation time, τ, is a combination of various scattering mechanisms such as grain boundary scattering (τ_{GB}), point defect scattering (τ_{PD}), Umklapp scattering (τ_U), and electron phonon scattering (τ_{EP}) as expressed using the Matthiessen's rule in eq 5.[53] Details of the fitting parameters along with calculation of θ_D, τ, and v_m are shown in Table S6, Supporting Information.

$$\tau^{-1} = \tau_{GB}^{-1} + \tau_{PD}^{-1} + \tau_U^{-1} + \tau_{EP}^{-1}$$
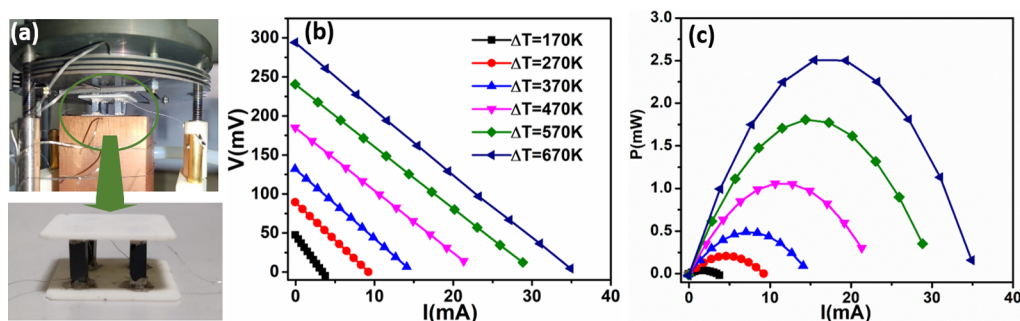$$= \frac{v_m}{L} + A\omega^4 + B\omega^2 T e^{-\theta_D/3T} + C\omega^2 \qquad (5)$$

Figure 5. Thermoelectric device measurement: (a) image of the four-legged n-type module, (b) I−V curve, and (c) power output with current at different temperatures.

It is evident from Table S7 and the inset of (Figure 4b) that Umklapp scattering is dominating, and it increases with graphite addition. Graphite−LSTN grain interfaces help it to produce more phonon modes, which further lead to enhanced phonon−phonon Umklapp scattering. However, it decreases at a higher graphite concentration (2 wt %) due to agglomeration of graphite. Electron phonon scattering is also found to be increased slightly due to graphite incorporation in LSTN.

ZT is calculated for all the compositions. A maximum ZT of 0.68 has been obtained at 980 K for the LSTN + 1 wt % G composition, which is five times higher than the maximum ZT obtained for pristine $La_{0.07}Sr_{0.93}Ti_{0.93}Nb_{0.07}O_3$ (ZT = 0.13). Both 0.5 wt % G and 1 wt % G composites of LSTN exhibit higher ZT values than the rest of the compositions. Maximum ZT reported for $La_{0.07}Sr_{0.93}Ti_{0.93}Nb_{0.07}O_3$ in the literature is 0.42 at 1000 K.[4] Therefore, it suggests more headroom for ZT enhancement. The quality factor (B) is estimated using eq 6[54,55] for all LSTN compositions. The quality factor increases with temperature for all compositions. A maximum quality factor of 0.24 is obtained for LSTN + 1 wt % G at 980 K.

$$B = \left(\frac{k_B}{e}\right)^2 \frac{8\pi e (2m_e k_B T)^{3/2}}{3h^3} \bullet \frac{\mu_w}{\kappa_l} T \tag{6}$$

Device Fabrication. A TEG with four n-type legs (3 mm × 3 mm × 8 mm of LSTN + 1 wt % G) is fabricated as shown in Figure 5a for checking its power generation capability. Two alumina plates with 0.5 mm thickness are used at both sides. Because we have used only n-type legs instead of the popular use of a n−p configuration, the device architecture is modified as shown schematically in Figure S8. Details of the device fabrication are given in the Supporting Information. In order to make all the legs electrically connected in series, silver wire goes from the top of one leg to the bottom of the next leg owing to the n-type unileg configuration. Silver paste is used to make all the connection with a silver wire. During the measurement, the cold end (bottom) temperature has been set to 300 K and the hot side temperature has been varied from 400 to 973 K. The entire measurement has been conducted at a low argon pressure. To the best of our knowledge, this is the first report to determine the power output in polycrystalline STO-based n-type unileg assembly. We have obtained a maximum open circuit voltage of 294 mV and a maximum power output (P_{total}) of 2.5 mW with the temperature difference (ΔT) maintained at 670 K between the hot and cold ends (Figure 5b,c). Even though we used only n-type legs, we have achieved a power output 15 times higher than that of the n-CaMnO$_3$ and p-Ca$_3$Co$_4$O$_9$ (∼160 μW) system.[21]

CONCLUSIONS

In summary, composites of $La_{0.07}Sr_{0.93}Ti_{0.93}Nb_{0.07}O_3$ with graphite (G) have been fabricated successfully using SPS. The presence of conductive graphite inclusions enhances the weighted mobility of electrons in the LSTN system. It is hypothesized that incorporation of graphite acts as the electron momentum booster helping the Anderson localized electrons in the LSTN system becoming itinerant. As a result, the electrical conductivity is enhanced by 5.2 times without sacrificing the Seebeck coefficient and eventually the power factor is increased by an order of magnitude for LSTN + 1 wt % G than that of pristine LSTN. At the same time, the presence of graphite also increases the phonon−phonon Umklapp scattering at an optimum graphite concentration. The maximum thermoelectric ZT is recorded to be 0.68 for LSTN + 1 wt % G at 980 K, which is about ∼423% larger than that of pristine LSTN. We have obtained about 2.5 mW of power output, which is much higher than the microwatt level of power output reported in the literature for oxide thermoelectrics. Further device level optimization is required to minimize the different losses in order to increase the power output of TEG. Because we have used only n-type thermo-electric legs in the present work, it is believed that the use of both n- and p-type oxide legs will be able to increase the power generation of TEG. Nevertheless, we have shown a strategy to improve the thermoelectric performance by forming an oxide composite with low−cost, easily available graphite for high-temperature thermoelectric power generation.

ASSOCIATED CONTENT

ⓢ Supporting Information

The Supporting Information is available free of charge at https://pubs.acs.org/doi/10.1021/acsami.1c24625.

> Synthesis and characterization of LSTN + G composites; Rietveld analysis of LSTN + 1 wt % G and refined parameters; lattice parameters of all the compositions; Raman spectroscopy; XPS spectra and binding energy; elemental mapping; UV spectra and band gaps; cyclability of electrical transport; carrier concentration by Hall measurement; Pisarenko plot; details of thermal conductivity measurement along with the Debye Call-away model; and schematic of device fabrication (PDF)

AUTHOR INFORMATION

Corresponding Author

Tanmoy Maiti − *Plasmonics and Perovskites Laboratory, Department of Materials Science and Engineering, IIT*

Kanpur, Kanpur, Uttar Pradesh 208016, India;
 orcid.org/0000-0003-1581-7614; Phone: +91-512-259-6599; Email: tmaiti@iitk.ac.in

Author

Subhra Sourav Jana − *Plasmonics and Perovskites Laboratory, Department of Materials Science and Engineering, IIT Kanpur, Kanpur, Uttar Pradesh 208016, India*

Complete contact information is available at:
https://pubs.acs.org/10.1021/acsami.1c24625

Notes

The authors declare no competing financial interest.

■ REFERENCES

(1) Tan, G.; Zhao, L.-D.; Kanatzidis, M. G. Rationally Designing High-Performance Bulk Thermoelectric Materials. *Chem. Rev.* **2016**, *116*, 12123−12149.

(2) Rahman, J. U.; Nam, W. H.; Van Du, N.; Rahman, G.; Rahman, A. U.; Shin, W. H.; Seo, W.-S.; Kim, M. H.; Lee, S. Oxygen Vacancy Revived Phonon-Glass Electron-Crystal in SrTiO3. *J. Eur. Ceram. Soc.* **2019**, *39*, 358−365.

(3) Wang, J.; Zhang, B.-Y.; Kang, H.-J.; Li, Y.; Yaer, X.; Li, J.-F.; Tan, Q.; Zhang, S.; Fan, G.-H.; Liu, C.-Y.; Miao, L.; Nan, D.; Wang, T.-M.; Zhao, L.-D. Record High Thermoelectric Performance in Bulk SrTiO3 via Nano-Scale Modulation Doping. *Nano Energy* **2017**, *35*, 387−395.

(4) Li, J.-B.; Wang, J.; Li, J.-F.; Li, Y.; Yang, H.; Yu, H.-Y.; Ma, X.-B.; Yaer, X.; Liu, L.; Miao, L. Broadening the Temperature Range for High Thermoelectric Performance of Bulk Polycrystalline Strontium Titanate by Controlling the Electronic Transport Properties. *J. Mater. Chem. C* **2018**, *6*, 7594−7603.

(5) Wu, C.; Li, J.; Fan, Y.; Xing, J.; Gu, H.; Zhou, Z.; Lu, X.; Zhang, Q.; Wang, L.; Jiang, W. the Effect of Reduced Graphene Oxide on Microstructure and Thermoelectric Properties of Nb-Doped A-Site-Deficient SrTiO3 Ceramics. *J. Alloys Compd.* **2019**, *786*, 884−893.

(6) Okhay, O.; Zlotnik, S.; Xie, W.; Orlinski, K.; Hortiguela Gallo, M. J.; Otero-Irurueta, G.; Fernandes, A. J. S.; Pawlak, D. A.; Weidenkaff, A.; Tkach, A. Thermoelectric Performance of Nb-Doped SrTiO3 Enhanced by Reduced Graphene Oxide and Sr Deficiency Cooperation. *Carbon* **2019**, *143*, 215−222.

(7) Lin, Y.; Norman, C.; Srivastava, D.; Azough, F.; Wang, L.; Robbins, M.; Simpson, K.; Freer, R.; Kinloch, I. A. Thermoelectric Power Generation from Lanthanum Strontium Titanium Oxide at Room Temperature through the Addition of Graphene. *ACS Appl. Mater. Interfaces* **2015**, *7*, 15898−15908.

(8) Lin, Y.; Dylla, M. T.; Kuo, J. J.; Male, J. P.; Kinloch, I. A.; Freer, R.; Snyder, G. J. Graphene/Strontium Titanate: Approaching Single Crystal-Like Charge Transport in Polycrystalline Oxide Perovskite Nanocomposites through Grain Boundary Engineering. *Adv. Funct. Mater.* **2020**, *30*, 1910079.

(9) Feng, X.; Fan, Y.; Nomura, N.; Kikuchi, K.; Wang, L.; Jiang, W.; Kawasaki, A. Graphene Promoted Oxygen Vacancies in Perovskite for Enhanced Thermoelectric Properties. *Carbon* **2017**, *112*, 169−176.

(10) Dey, P.; Jana, S. S.; Anjum, F.; Bhattacharya, T.; Maiti, T. Effect of semiconductor to metal transition on thermoelectric performance in oxide nanocomposites of SrTi0.85Nb0.15O3 with graphene oxide. *App. Mater. Today* **2020**, *21*, 100869.

(11) Rahman, J. U.; Van Du, N.; Nam, W. H.; Shin, W. H.; Lee, K. H.; Seo, W.-S.; Kim, M. H.; Lee, S. Grain Boundary Interfaces Controlled by Reduced Graphene Oxide in Nonstoichiometric SrTiO3-δ Thermoelectrics. *Sci. Rep.* **2019**, *9*, 8624−12.

(12) Acharya, M.; Jana, S. S.; Ranjan, M.; Maiti, T. High performance (ZT>1) n-type oxide thermoelectric composites from earth abundant materials. *Nano Energy* **2021**, *84*, 105905.

(13) Tang, H.; Sun, F.-H.; Dong, J.-F.; Asfandiyar, H.-L.; Zhuang, H.-L.; Pan, Y.; Li, J.-F. Graphene Network in Copper Sulfide Leading to Enhanced Thermoelectric Properties and Thermal Stability. *Nano Energy* **2018**, *49*, 267−273.

(14) Ohta, S.; Nomura, T.; Ohta, H.; Koumoto, K. High-temperature carrier transport and thermoelectric properties of heavily La- or Nb-doped SrTiO3 single crystals. *J. Appl. Phys.* **2005**, *97*, 034106.

(15) Biswas, A.; Kim, K.-S.; Jeong, Y. H. Metal Insulator Transitions in Perovskite SrIrO3 Thin Films. *J. Appl. Phys.* **2014**, *116*, 213704.

(16) Gilbert, S. R.; Wills, L. A.; Wessels, B. W.; Schindler, J. L.; Thomas, J. A.; Kannewurf, C. R. Electrical Transport Properties of Epitaxial Batio3 Thin Films. *J. Appl. Phys.* **1996**, *80*, 969−977.

(17) Li, Y.; Liu, J.; Li, J.-C.; Chen, Y.-F.; Zhang, X.-M.; Wang, X.-J.; Wang, F.-N.; Su, W.-B.; Zhao, L.-L.; Wang, C.-L. Electron localization in niobium doped CaMnO3 due to the energy difference of electronic states of Mn and Nb. *Phys. Chem. Chem. Phys.* **2018**, *20*, 20571−20574.

(18) Lee, S.; Bock, J. A.; Trolier-Mckinstry, S.; Randall, C. A. Ferroelectric-Thermoelectricity and Mott Transition of Ferroelectric Oxides with High Electronic Conductivity. *J. Eur. Ceram. Soc.* **2012**, *32*, 3971−3988.

(19) Maiti, T.; Saxena, M.; Roy, P. Double Perovskite (Sr 2 B′ B ″O 6) Oxides for High-Temperature Thermoelectric Power Generation—A Review. *J. Mater. Res.* **2018**, *34*, 107.

(20) Roy, P.; Waghmare, V.; Tanwar, K.; Maiti, T. Large change in thermopower with temperature driven p-n type conduction switching in environment friendly BaxSr2−xTi0.8Fe0.8Nb0.4O6 double perovskites. *Phys. Chem. Chem. Phys.* **2017**, *19*, 5818−5829.

(21) Bose, R. S. C.; Nag, A. Investigation of Thermoelectric Performance and Power Generation Characteristics of Dual-Doped Ca1-xRE′x/2RE″x/2MnO3 (RE′/RE″ = Dy, Gd, Yb, Lu; 0.05 ≤ x ≤ 0.1). *ACS Appl. Energy Mater.* **2018**, *1*, 3151−3158.

(22) Ferrari, A. C.; Robertson, J. Interpretation of Raman Spectra of Disordered and Amorphous Carbon. *Phys. Rev. B: Condens. Matter Mater. Phys.* **2000**, *61*, 14095.

(23) Marković, Z.; Budimir, M.; Kepić, D.; Holclajtner-Antunović, I.; Marinović-Cincović, M.; Dramićanin, M.; Spasojević, V.; Peruško, D.; Špitalský, Z.; Mičušik, M. Semi-Transparent, Conductive Thin Films of Electrochemical Exfoliated Graphene. *RSC Adv.* **2016**, *6*, 39275−39283.

(24) Balasubramanyan, S.; Sasidharan, S.; Poovathinthodiyil, R.; Ramakrishnan, R. M.; Narayanan, B. N. Sucrose-Mediated Mechanical Exfoliation of Graphite: A Green Method for the Large Scale Production of Graphene and its Application in Catalytic Reduction of 4-Nitrophenol. *New J. Chem.* **2017**, *41*, 11969−11978.

(25) Kim, H. J.; Lee, S.-M.; Oh, Y.-S.; Yang, Y.-H.; Lim, Y. S.; Yoon, D. H.; Lee, C.; Kim, J.-Y.; Ruoff, R. S. Unoxidized Graphene/Alumina Nanocomposite: Fracture- and Wear-Resistance Effects of Graphene on Alumina Matrix. *Sci. Rep.* **2014**, *4*, 5176.

(26) Marshall, M. S. J.; Newell, D. T.; Payne, D. J.; Egdell, R. G.; Castell, M. R. Atomic and Electronic Surface Structures of Dopants in Oxides: STM and XPS of Nb-And La-Doped SrTiO 3 (001). *Phys. Rev. B: Condens. Matter Mater. Phys.* **2011**, *83*, 035410.

(27) Bharti, B.; Kumar, S.; Lee, H.-N.; Kumar, R. J. S. R. Formation of Oxygen Vacancies and Ti 3+ State in TiO 2 Thin Film And Enhanced Optical Properties by Air Plasma Treatment. *Sci. Rep.* **2016**, *6*, 1−12.

(28) Wagner, C. D. *Nist X-ray Photoelectron Spectroscopy Database*; NIST Standard Reference Database, 2000.

(29) Bhaskar, S.; Allgeyer, D.; Smythe, J. A., III Depth profiling of dielectric SrTiO3 thin films by angle-resolved x-ray photoelectron spectroscopy. *Appl. Phys. Lett.* **2006**, *89*, 254103.

(30) Chu, C. M.; Wu, J. J.; Yung, S. W.; Chin, T. S.; Zhang, T.; Wu, F. B. Optical and structural properties of Sr-Nb-phosphate glasses. *J. Non-Cryst. Solids* **2011**, *357*, 939−945.

(31) Ohta, S.; Nomura, T.; Ohta, H.; Hirano, M.; Hosono, H.; Koumoto, K. Large thermoelectric performance of heavily Nb-doped SrTiO3 epitaxial film at high temperature. *Appl. Phys. Lett.* **2005**, *87*, 092108.

(32) Wang, N.; He, H.; Ba, Y.; Wan, C.; Koumoto, K. Thermoelectric Properties of Nb-Doped SrTiO3 Ceramics Enhanced by Potassium Titanate Nanowires Addition. *J. Ceram. Soc. Jpn.* **2010**, *118*, 1098−1101.

(33) Ohta, S.; Nomura, T.; Ohta, H.; Koumoto, K. High-temperature carrier transport and thermoelectric properties of heavily La- or Nb-doped SrTiO3 single crystals. *J. Appl. Phys.* **2005**, *97*, 034106.

(34) Roy, P.; Waghmare, V.; Maiti, T. Environmentally friendly BaxSr2−xTiFeO6double perovskite with enhanced thermopower for high temperature thermoelectric power generation. *RSC Adv.* **2016**, *6*, 54636−54643.

(35) Sudha; Saxena, M.; Balani, K.; Maiti, T. Structure and Thermoelectric Properties of Calcium Doped Sr2TiCoO6 Double Perovskites. *Mater. Sci. Eng. B* **2019**, *244*, 65−71.

(36) Saxena, M.; Maiti, T. Effect of Ba-doping on high temperature thermoelectric properties of Sr2TiMoO6 double perovskites. *J. Alloys Compd.* **2017**, *710*, 472−478.

(37) Bock, J. A.; Trolier-Mckinstry, S.; Mahan, G. D.; Randall, C. A. Polarization-based perturbations to thermopower and electronic conductivity in highly conductive tungsten bronze structured(Sr,Ba)-Nb2O6: Relaxors vs normal ferroelectrics. *Phys. Rev. B: Condens. Matter Mater. Phys.* **2014**, *90*, 115106.

(38) Lee, S.; Yang, G.; Wilke, R. H. T.; Trolier-Mckinstry, S.; Randall, C. A. Thermopower in highly reducedn-type ferroelectric and related perovskite oxides and the role of heterogeneous non-stoichiometry. *Phys. Rev. B: Condens. Matter Mater. Phys.* **2009**, *79*, 134110.

(39) Mott, N. F. The Basis Of The Electron Theory of Metals, with Special Reference to the Transition Metals. *Proc. Phys. Soc., London, Sect. A* **1949**, *62*, 416.

(40) Cox, P. A. *Transition Metal Oxides: An Introduction to Their Electronic Structure and Properties*; Oxford University Press, 2010; Vol. 27.

(41) Bjaalie, L.; Janotti, A.; Himmetoglu, B.; Van De Walle, C. G. TurningSrTiO3into a Mott insulator. *Phys. Rev. B: Condens. Matter Mater. Phys.* **2014**, *90*, 195117.

(42) Okuda, T.; Nakanishi, K.; Miyasaka, S.; Tokura, Y. Large Thermoelectric Response of Metallic Perovskites: Sr 1− X La X Tio 3 (0<∼ X<∼ 0. 1). *Phys. Rev. B: Condens. Matter Mater. Phys.* **2001**, *63*, 113104.

(43) Wunderlich, W.; Ohta, H.; Koumoto, K. Enhanced Effective Mass in Doped SrTiO3 and Related Perovskites. *Phys. B* **2009**, *404*, 2202−2212.

(44) Lee, C.; Destry, J.; Brebner, J. L. Optical absorption and transport in semiconducting SrTiO3. *Phys. Rev. B: Condens. Matter Mater. Phys.* **1975**, *11*, 2299.

(45) Anderson, P. W. Absence of Diffusion in Certain Random Lattices. *Phys. Rev.* **1958**, *109*, 1492.

(46) Bernasconi, P.; Biaggio, I.; Zgonik, M.; Günter, P. Anisotropy of the Electron and Hole Drift Mobility inKNbO3andBaTiO3. *Phys. Rev. Lett.* **1997**, *78*, 106.

(47) Ihrig, H.; Hennings, D. Electrical transport properties ofn-type BaTiO3. *Phys. Rev. B: Condens. Matter Mater. Phys.* **1978**, *17*, 4593.

(48) Li, Y.; Liu, J.; Li, J.-C.; Chen, Y.-F.; Zhang, X.-M.; Wang, X.-J.; Wang, F.-N.; Su, W.-B.; Zhao, L.-L.; Wang, C.-L. Electron localization in niobium doped CaMnO3 due to the energy difference of electronic states of Mn and Nb. *Phys. Chem. Chem. Phys.* **2018**, *20*, 20571−20574.

(49) Kittel, C.; Mceuen, P.; Mceuen, P. *Introduction to Solid State Physics*; Wiley: New York, 1996; Vol. 8.

(50) Kim, H.-S.; Gibbs, Z. M.; Tang, Y.; Wang, H.; Snyder, G. J. Characterization of Lorenz Number with Seebeck Coefficient Measurement. *Apl. Mater.* **2015**, *3*, 041506.

(51) Cahill, D. G.; Watson, S. K.; Pohl, R. O. Lower Limit to the Thermal Conductivity of Disordered Crystals. *Phys. Rev. B: Condens. Matter Mater. Phys.* **1992**, *46*, 6131.

(52) Callaway, J. Model for Lattice Thermal Conductivity at Low Temperatures. *Phys. Rev.* **1959**, *113*, 1046.

(53) Rahman, J. U.; Nam, W. H.; Van Du, N.; Rahman, G.; Rahman, A. U.; Shin, W. H.; Seo, W.-S.; Kim, M. H.; Lee, S. Oxygen Vacancy Revived Phonon-Glass Electron-Crystal in SrTiO3. *J. Eur. Ceram. Soc.* **2019**, *39*, 358−365.

(54) Zevalkink, A.; Smiadak, D. M.; Blackburn, J. L.; Ferguson, A. J.; Chabinyc, M. L.; Delaire, O.; Wang, J.; Kovnir, K.; Martin, J.; Schelhas, L. T.; Sparks, T. D.; Kang, S. D.; Dylla, M. T.; Snyder, G. J.; Ortiz, B. R.; Toberer, E. S. A Practical Field Guide to Thermo-electrics: Fundamentals, Synthesis, and Characterization. *Appl. Phys. Rev.* **2018**, *5*, 021303.

(55) Pei, Y.; Wang, H.; Snyder, G. J. Band Engineering of Thermoelectric Materials. *Adv. Mater.* **2012**, *24*, 6125−6135.

▣ Recommended by ACS